nature nanotechnology

LETTERS

PUBLISHED ONLINE: 19 JUNE 2011 | DOI: 10.1038/NNANO.2011.88

Single-molecule transport across an individual biomimetic nuclear pore complex

Stefan W. Kowalczyk[1], Larisa Kapinos[2], Timothy R. Blosser[1], Tomás Magalhães[1], Pauline van Nies[1], Roderick Y. H. Lim[2]* and Cees Dekker[1]*

Nuclear pore complexes regulate the selective exchange of RNA and proteins across the nuclear envelope in eukaryotic cells[1]. Biomimetic strategies offer new opportunities to investigate this remarkable transport phenomenon[2]. Here, we show selective transport of proteins across individual biomimetic nuclear pore complexes at the single-molecule level. Each biomimetic complex is constructed by covalently tethering either Nup98 or Nup153 (phenylalanine-glycine (FG) nucleoporins) to a solid-state nanopore[3]. Individual translocation events are monitored using ionic current measurements with sub-millisecond temporal resolution. Transport receptors (Impβ) proceed with a dwell time of ∼2.5 ms for both Nup98- and Nup153-coated pores, whereas the passage of non-specific proteins is strongly inhibited with different degrees of selectivity. For pores up to ∼25 nm in diameter, Nups form a dense and low-conducting barrier, whereas they adopt a more open structure in larger pores. Our biomimetic nuclear pore complex provides a quantitative platform for studying nucleocytoplasmic transport phenomena at the single-molecule level *in vitro*.

The nuclear pore complex (NPC) is the sole connection between the nucleus and the cytosol of eukaryotic cells. By connecting the genetic material and the protein-synthesizing apparatus, this remarkable 'gatekeeper'[4] regulates all nucleocytoplasmic transport. The NPC acts as a selective sieve that is permeable to ions and small solutes (up to ∼40 kDa), while macromolecular access is reserved for transport receptors (karyopherins) that ferry cargo. Vertebrate NPCs have a total mass of ∼120 MDa and are composed of ∼30 distinct protein subunits (nucleoporins or Nups)[5]. Approximately one-third of these Nups contain natively unfolded FG domains[6] that are rich in mainly FxFG or GLFG repeat motifs (F-Phe; G-Gly; L-Leu; x-any amino acid). Importantly, the FG-domains are believed to constitute the key NPC components that regulate the selective access of receptor–cargo complexes across the NPC channel[7].

There is a need to test the various models that have been proposed for the mechanism of transport. Current NPC transport models include the 'virtual-gate'[8,9], 'polymer-brush'[10], 'selective-phase'[11,12] and 'reduction-of-dimensionality'[13] models. It has been argued that both brush-like (less cohesive FxFG domains) and meshwork-like (more cohesive GLFG domains) Nup conformations are present in the NPC[14]. Despite recent experimental efforts[15], it remains a challenge to discriminate between NPC models due to the complexity of the cellular environment. It would be useful to reconstitute the large NPC *in vitro*, where conditions and parameters can be changed systematically, but this has proven impossible. It has thus remained a challenge to probe selective transport at the relevant length and time scales.

In this Letter, we take a bottom-up approach that enables single-molecule transport studies on a biomimetic 'minimalist NPC' *in vitro*. We constructed biomimetic NPCs by tethering FG Nups to individual solid-state nanopores. This follows bulk selective transport experiments through parallel ($\sim 1 \times 10^8$) artificial NPCs constructed from polymeric membranes[2] and functionalized long nanochannels[16–19]. The first step in our bottom-up approach[20] involved drilling a small hole (nanopore) in a thin free-standing silicon nitride (SiN) membrane with a focused transmission electron microscope (TEM) beam (see Fig. 1a and Methods)[3,21]. Subsequently, Nup functionalization of the nanopore was performed in a three-step process similar to the immobilization of DNA to silicon surfaces[22] (see Supplementary Information for details). Representative TEM images (Fig. 1c) confirmed the presence of organic material after coating a nanopore with Nups. Note that we worked with truncated versions of Nup98 and Nup153 that are limited to the relevant FG domains (see Materials and Methods). The SiN membrane was placed in a microfluidic flow cell where a single nanopore formed the only connection between two compartments (Fig. 1b). Subsequently we measured the transport properties of our biomimetic NPC. In the past, electrical measurements were performed on the nuclear envelope[23,24], but these remain subject to dispute in the light of technical issues with sealing of the nuclear membrane.

Ion current measurements through a 40 nm pore in near-physiological salt conditions (Fig. 1d) revealed an increased resistance (decreased conductance) on coating the pore with Nup98, which partially blocks the pore and reduces the ion conductance. The strictly linear current–voltage (I–V) characteristics indicate that the Nups are not aligned by the applied electric field (in accordance with their low charge; Supplementary Table T1 and Section S5), which merely acts as a non-invasive probe. We estimate the Nup density to be ∼1 Nup per 50 nm^2 along the circumference of the pore (Supplementary Section S3). Given the hydrodynamic diameter of these proteins (∼11 nm) this is a very-high-density (close to monolayer) coverage. Current power spectral densities[25] show comparable noise levels at high frequencies with an increased $1/f$-type low-frequency noise for the NPC mimics compared to the bare pores (Supplementary Section S6). This can probably be attributed to the dynamic fluctuations of Nups, similar to reports for the motion of polymeric subunits in a nanopore[26].

Figure 2a compares the measured conductance for bare (black squares), Nup98- (green circles) and Nup153-coated pores (inset, red triangles) over a wide range of pore diameters. Three observations stand out. First, the conductance decreases in the presence of Nups regardless of pore size. Second, Nup98 has a stronger effect on lowering the conductance than Nup153. Third, and surprisingly, the pore conductance remains almost negligible up to ∼25 nm, followed by a rise with a slope that is roughly similar to that of bare pores.

[1]Kavli Institute of Nanoscience, Delft University of Technology, Lorentzweg 1, 2628 CJ Delft, The Netherlands, [2]Biozentrum and the Swiss Nanoscience Institute, University of Basel, Klingelbergstrasse 70, CH-4056 Basel, Switzerland. *e-mail: roderick.lim@unibas.ch; c.dekker@tudelft.nl

© 2011 Macmillan Publishers Limited. All rights reserved.

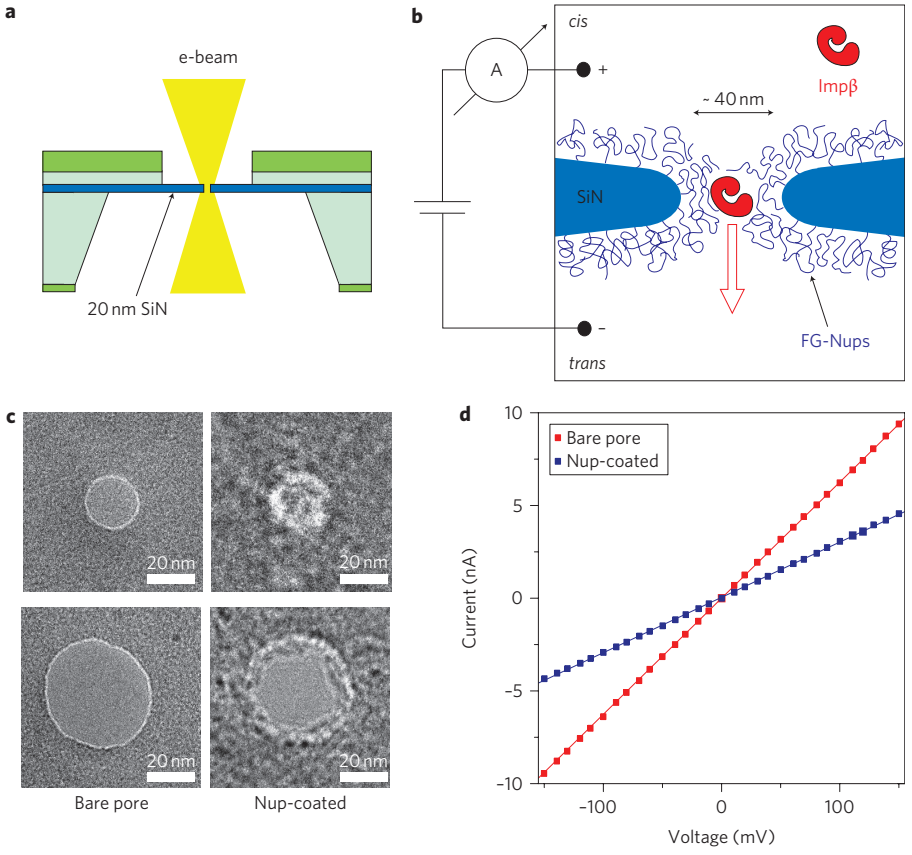

Figure 1 | Biomimetic NPC. a, Side-view schematic showing the device consisting of a 20 nm thin, free-standing silicon nitride window (blue layer) embedded in a silicon wafer (light green). A nanopore is drilled using a highly focused electron beam (yellow). **b**, Sketch showing the experimental concept. The biomimetic NPC is engineered by attaching FG-Nups to a solid-state nanopore, and transport of Impβ is measured by monitoring the trans-pore current. **c**, TEM images of the same nanopore with a diameter of 20 nm (top) or 40 nm (bottom) before (left) and after (right) coating with Nup98. **d**, Example of a current–voltage (I–V) curve before (red) and after (blue) coating a 40 nm nanopore with Nup98, showing an increased resistance due to the coating.

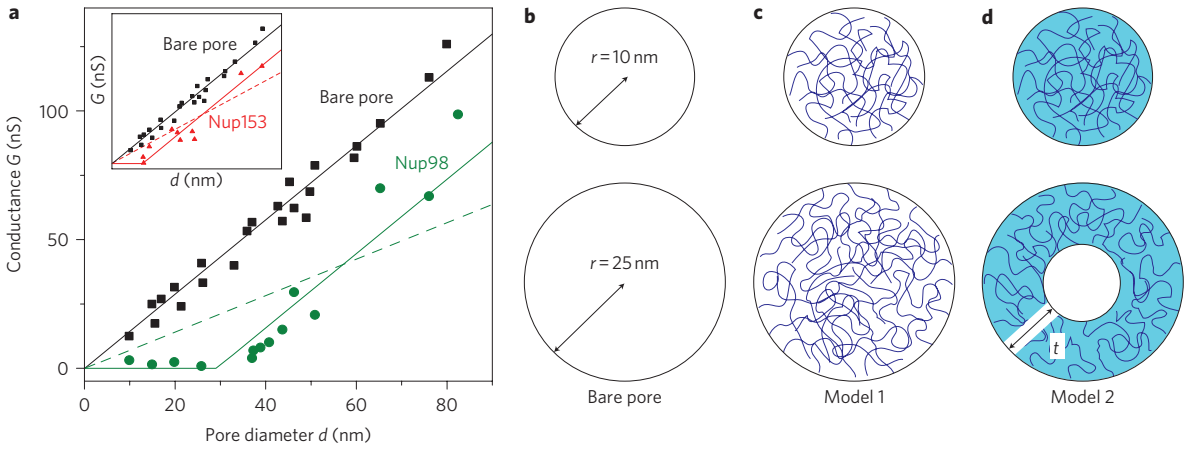

Figure 2 | Conductance measurements and models. a, Measured conductance versus pore diameter for bare pores (black points), Nup98-coated (green) and Nup153-coated (inset, red) pores. For all pores, the pore conductance decreases upon coating. Coloured lines are linear fits of two models (see text). Model 2 (solid lines) is found to fit the data much better than model 1 (dashed lines). **b**–**d**, Schematics showing small- and large-pore regimes for models 1 and 2, as discussed in the text. Fitting to model 2 yields a Nup layer thickness $t_{Nup98} = 15 \pm 1$ nm and $t_{Nup153} = 8 \pm 1$ nm along the circumference of the pore for Nup98 and Nup153, respectively.

We discuss two simple models that may potentially account for these data. In model 1, the pore is filled with a Nup meshwork with multiple channels of some characteristic size, corresponding to the selective-phase model[11,12] (Fig. 2c). This gives rise to a finite ionic permeability, which is a material parameter that is independent of nanopore diameter. Accordingly, model 1 exhibits a linear conductance[27] as a function of pore diameter (Fig. 2a, dashed line) as given by $G(r) = \gamma G_0(r)$, where G_0 is the bare pore conductance, γ is a fraction that denotes the reduction of the conduction, and r is the pore radius. This yields an effective ion permeability of

© 2011 Macmillan Publishers Limited. All rights reserved.

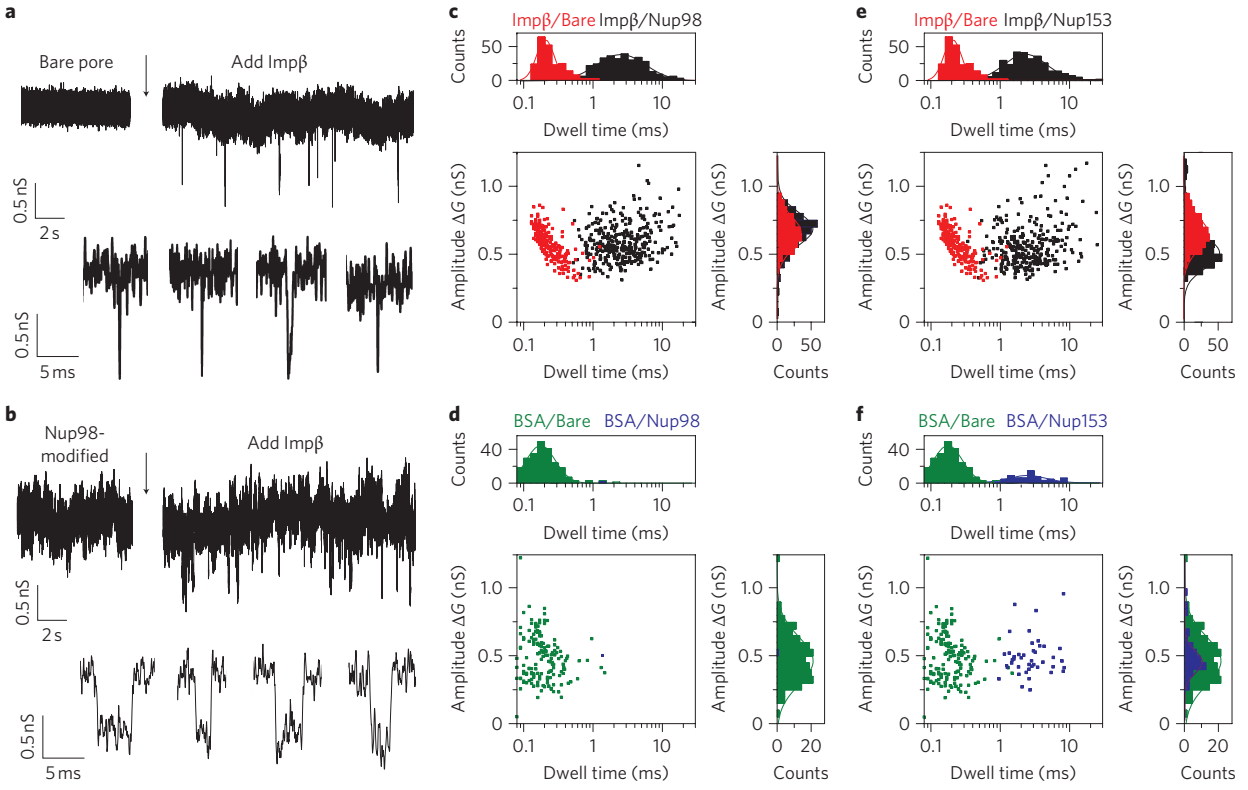

Figure 3 | Single-molecule translocation events. a, Representative ion current trace before and after addition of Impβ in a bare pore. Downward spikes appear in the current trace upon addition of Impβ. Each spike is a single-molecule event. The lower panel shows zoom-ins on a number of events. **b**, As in **a**, but for a Nup98-coated pore. **c**, Scatter diagram for Impβ translocation in a bare (red) and Nup98-modified (black) pore, where each point represents an individual event. Event amplitudes are similar (~0.6 nS), but the dwell times differ by more than an order of magnitude (~200 μs versus ~3 ms). **d**, Scatter diagram for BSA translocation through bare (green) and Nup98 pores (black). **e**, As in **c**, but for a Nup153 pore. **f**, As in **d**, but for a Nup153-modified pore.

$\gamma = 50\%$ for Nup98 and $\gamma = 67\%$ for Nup153 (defining the permeability of a bare pore as 100%). However, this provides a very poor fit to the data with a normalized reduced sum of squared residuals $\chi^2 = 16.7$ and 8.1 for Nup98 and Nup153, respectively.

In model 2, the Nups coat the circumference of a pore with a dense layer of thickness t (that we assume, to first order, not to significantly conduct ions), leaving an open channel through the central pore axis that is available for ion conduction (Fig. 2d). For small pores ($r < t$), the high density of Nups occludes the entire channel, thereby blocking ion conduction ($G \approx 0$). For large pores ($r > t$), a more open central channel is formed based on the difficulty for opposing Nups to stretch and crosslink each other across the pore. This conductance is given by $G(r) = G_0(r-t)$, that is, a linear dependence on pore diameter beyond an offset of 29 ± 2 nm for Nup98-coated pores and 16 ± 2 nm for Nup153-coated pores (solid lines in Fig. 2a and inset). Model 2 fits the data much better, with $\chi^2 = 3.8$ and 3.6 for Nup98 and Nup153, respectively. The horizontal offsets correspond to $t_{\mathrm{Nup98}} = 15 \pm 1$ nm and $t_{\mathrm{Nup153}} = 8 \pm 1$ nm along the pore circumference. Note that these two models are limiting cases only. Other Nup arrangements with equal excluded conducting areas are also possible (Supplementary Fig. S8). Indeed, the Nups could resemble some subtle mixture of models 1 and 2, where some low density of dynamic Nups is present at the pore centre. Nevertheless, model 2 is close to recent descriptions of Nups within the NPC[28,29].

An important question is whether these minimal hybrid nanopores indeed mimic NPCs. To test for the most discriminating characteristic, selectivity, we compared the transport properties of Impβ (97 kDa) and bovine serum albumin (BSA, a 66 kDa protein with similar charge and isoelectric point, see Supplementary Section S4) through 40-nm-diameter pores. Using first a bare pore as a control, we observe downward spike-like changes in the open-pore conductance after adding either Impβ or BSA to the *cis* side (Fig. 3a). Each spike signals the translocation of an individual protein[3,30]. Subsequently, we repeated these experiments on Nup-modified pores. Figure 3b shows representative traces of Impβ translocations through Nup98-coated pores (and similarly, Supplementary Fig. S9 for Nup153-coated pores). Short temporal depressions in the current again appear after adding Impβ. To our knowledge, these are the first single-molecule measurements of protein transport across individual biomimetic NPCs. An analysis of inter-event times (see Supplementary Section 9) indicates that $\sim 86 \pm 4\%$ of the observed events (spikes) are indeed translocations rather than binding events where the protein does return to the *cis* chamber. This corresponds well with single-molecule fluorescence studies that showed that ~20% of Impβ translocations were aborted after entering into the NPC[31].

We continue with a detailed quantification of the amplitudes and dwell times of these translocation events, using a standard event-fitting algorithm as described previously[32] (Supplementary Table T2). Each event is plotted in a scatter diagram of ΔG versus τ, where ΔG is the conductance blockade amplitude and τ the dwell time (Fig. 3c–f). Note that the average ΔG for Impβ is similar for a bare (0.59 ± 0.12 nS), a Nup98-coated (0.56 ± 0.12 nS) and a Nup153-coated pore (0.50 ± 0.10 nS). This is expected because ΔG is a measure of the size of the translocating object. The Impβ dwell time through a bare pore is short: a log-normal fit to the data gives 190 ± 40 μs (Fig. 3e, top histogram), in good agreement with previous reports of translocations of similar-sized proteins through solid-state nanopores[30]. As expected, comparable values (0.47 ± 0.19 nS; 170 ± 70 μs) were obtained for BSA translocation through a bare pore (Fig. 3d).

© 2011 Macmillan Publishers Limited. All rights reserved.

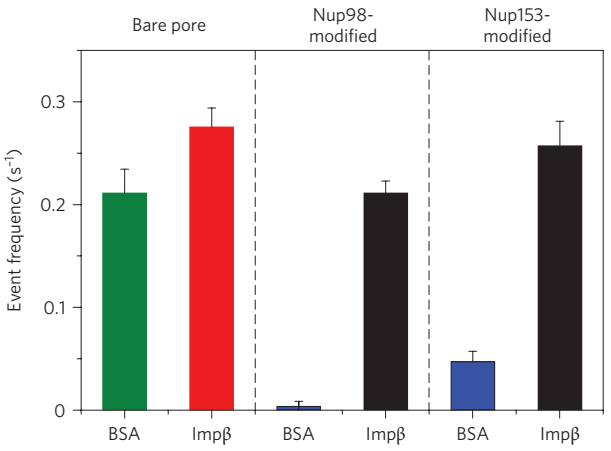

Figure 4 | Event frequencies through bare and Nup-modified pores, showing NPC-like selectivity. Average number of events per second for BSA through a bare pore (green), Impβ through a bare pore (red), BSA through a Nup98-coated pore (blue), Impβ through a Nup98-coated pore (black), and finally BSA through a Nup153-coated pore (blue) and Impβ through a Nup153-coated pore (black). Pore diameter is 42–46 nm in all cases. The passage of BSA through the Nup-modified pore is significantly inhibited in Nup-coated pores, whereas that of Impβ is not; that is, these pores display the hallmark of NPC selectivity.

Interestingly, we measured much longer dwell times for the passage of Impβ through Nup-coated pores: 2.7 ± 0.3 ms (average value from independent measurements on three different pores, $N = 3$) for a Nup98-coated pore (Fig. 3e) and 2.2 ± 0.3 ms (also $N = 3$) for a Nup153-coated pore (Fig. 3f). This is more than a 10-fold increase in dwell time compared to the bare pore. Remarkably, these values are in close agreement with the ~5 ms dwell time of Impβ in NPCs obtained by single-molecule fluorescence *in vivo*[33] and in permeabilized cells[28,34,35] (Supplementary Fig. S12). This indicates that Impβ interacts with the Nups for a substantial amount of time before exiting the pore. An important control is our observation that the dwell time is independent of the applied voltage (Supplementary Fig. S5b). This contrasts with conventional biomolecular transport through bare pores where the dwell time is inversely proportional to the applied voltage[36], and it shows that the ~2.5 ms time is intrinsically due to the Impβ–Nup interaction.

It is noteworthy that our simple biomimetic NPCs display the exclusive selectivity of native NPCs. A comparison of the event rates of BSA and Impβ translocation through a 46 nm pore before and after Nup98 modification is shown in Fig. 4. Most strikingly, the passage of BSA shows a dramatic 60-fold reduction in event rate, yielding 0.21 events/s in a bare pore but only 0.0035 events/s in the Nup98-coated pore. In contrast, the event rate for Impβ is similar in bare pores and Nup98-coated pores (0.27 versus 0.21 events/s). The biomimetic Nup98-coated pore thus very effectively blocks the passage of BSA, while the event frequency for Impβ is not significantly affected. For a 42-nm-diameter Nup153-coated pore, translocation of BSA and Impβ yielded rates of 0.05 and 0.25 events/s, respectively. This indicates that Nup98 hinders BSA transport more strongly than Nup153, although both Nups support similar Impβ event rates. Indeed, sequence analysis[14] indicates that Nup98 is more cohesive than Nup153 (Supplementary Table T3), providing for a more effective physical barrier. The reduced selectivity is also consistent with our finding (Fig. 2d) that the layer of Nup153 was thinner than that of the Nup98-coated pore. Nevertheless, our findings indicate that a single Nup is enough to form a barrier, and that intrinsic differences between Nups result in varying barrier effectiveness. Additional enhancement of transport selectivity might be achieved through competition of transport receptors and non-specific cargo[2,37,38].

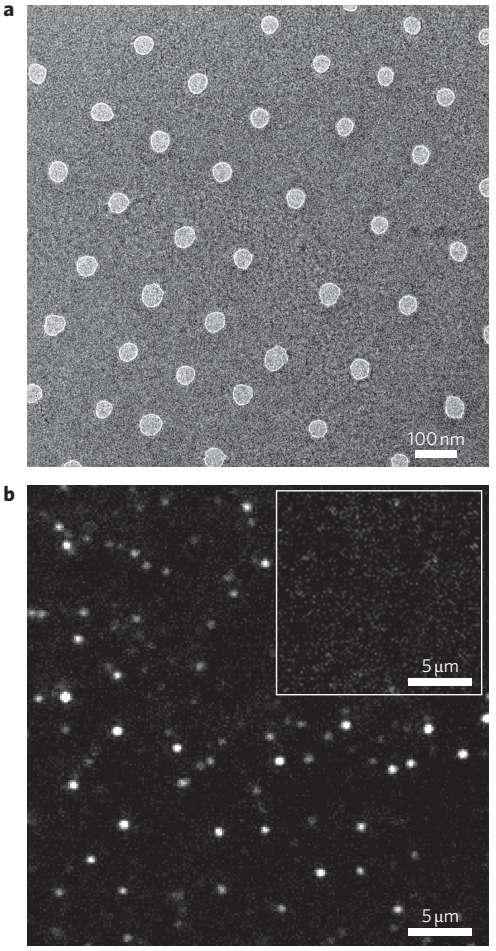

Figure 5 | Nanopore array. a, TEM image of a nanopore array consisting of 61 pores with diameters of 43 ± 3 nm. **b**, TIRF image of individual Alexa488-labelled fluorescent Impβ proteins that were translocated through the Nup98-coated nanopore array of **a** to the *trans* chamber and subsequently immobilized onto a cover slide (see text). The inset shows a control image of buffer only, for exactly the same TIRF conditions.

Finally, we used Alexa488-labelled Impβ to verify that Impβ proteins actually translocate through our Nup-coated pores to the *trans* chamber. Here we translocated proteins for 20 h through an array of 61 parallel Nup98-coated nanopores with diameters of 43 ± 3 nm (Fig. 5a and Supplementary Section 13) to maximize the amount of translocated Impβ in the *trans* chamber. Subsequently, buffer from the 20 μl *trans* chamber was deposited on a cover slide for total internal reflection fluorescence (TIRF) imaging (see Methods). Fluorescent proteins are clearly observed (Fig. 5b), corresponding to an amount of ~1 pM of Impβ that translocated to the *trans* chamber. This is in good agreement with the expected value of ~2 pM (Supplementary Section 14).

To conclude, we have built a *de novo* designed 'minimalist NPC' that faithfully reproduces the essential feature of selectivity of the NPC. We have used electrophysiology as a new technique to measure ion and protein transport across the biomimetic pore with single-molecule resolution. We have found that translocation events through such biomimetic NPCs are indeed observed for transport receptors (Impβ), whereas the passage of non-specific proteins (BSA) is strongly inhibited. Importantly, our approach has the advantage of revealing intrinsic differences between Nups that can determine the selectivity barrier. Future work may

© 2011 Macmillan Publishers Limited. All rights reserved.

encompass a stepwise expansion of the complexity of the system, as well as measurement of forces on transport factors during translocation using an integrated nanopore-optical tweezers setup[39].

Methods

Cloning and expression of recombinant Nup153 and Nup98. The 601aa C-terminal FG-repeat domain of human Nup153 (aa 874–1,475, Nup153-C) was PCR-cloned into bacterial expression vector pGEX 6P-1 (GE Healthcare), which contains a N-terminal glutathione-*S*-transferase (GST) and C-terminal His-tag. The nucleotide sequence encoding the FG-domains of human nucleoporin Nup98 (aa 1–505) was cloned into pPEP-TEV vector at the *Bam*HI and *Eco*RI restriction sites using the prokaryotic expression vector pPEP-TEV[40]. This construct contains a N-terminal His-tag followed by 36 residues of a short laminin linker and a TEV protease cleavage site. To allow attachment of the recombinant Nup153 or Nup98 fragments to the gold surfaces, three cysteines were added to the N-terminus in both cases. The recombinant Cys-Nup153 and Cys-Nup98 were expressed in *Escherichia coli* BL21 (DE3) competent cells (Novagen). The expressed FG-domains were purified under denaturing conditions (8 M urea, 100 mM Na_2HPO_4, 10 mM DTT and 10 mM Tris-HCl, pH 8.5) using a Ni-NTA column. A PreScision protease (GE Healthcare) was used to cleave both the N-terminal glutathione-*S*-transferase (GST) and C-terminal His-tag from Cys-Nup153-C after purification. TEV protease was used to remove the His-tag from Cys-Nup98. After cleavage, the recombinant fragments of Nup98 carry a pre-sequence of GlyGlySer before the three cysteines at the N-terminus. Some additional residues were also present in the Cys-Nup153-C construct at both termini after cleavage. Subsequently, all FG-domains were purified under denaturing conditions as done previously[11]. The His-tag-free protein fragments were than eluted with a buffer containing 8 M urea, 100 mM Na_2HPO_4, 10 mM DTT and 10 mM Tris-HCl, pH 8.5. The final protein purity was analysed by 12% PAGE at 0.1% SDS. The protein concentration was determined by Bradford assay and verified by estimation of protein amounts on Commassie Brilliant Blue-stained SDS-PAGE (12% acryl amide) (Supplementary Fig. S2). Alternatively, the protein concentration was also calculated from the absorption at 280 nm. An extinction coefficient of the protein fragment was calculated using the ProtParam program (available at ExPaSy homepage, http://us.expasy.org/sprot/).

Cloning and expression of Impβ. Full-length human Impβ was amplified by PCR and inserted into a *Nco*I–*Bam*HI digested pETM-11 expression vector (EMBL Protein Expression and Purification Facility). N-terminal His_6-tagged Impβ was expressed in *E. coli* BL21 (DE3) cells at 30 °C overnight and purified on a Ni-NTA column (50 mM TrisHCl, pH 8, 100 mM NaCl, 1 mM DTT; eluted with 80–300 mM imidazole) followed by gel-filtration using Superdex 200 column (GE Healthcare). Purified protein was analysed by SDS–PAGE (Supplementary Fig. S2) and selected fractions containing Impβ were pooled, dialysed against PBS and concentrated. Impβ was also labelled with Alexa Fluor488 sulphodichlorophenol esters (Alexa Fluor488-5-SDP ester) using a standard labelling procedure of Invitrogen Protocols for amine-reactive probes (http://products.invitrogen.com/ivgn/product/A30052). Labelling was carried out in PBS buffer with pH 7.2. Under these conditions, dye molecules couple mainly to the N-terminus (primary amine) of Impβ, and the amine groups of the side chains remain mainly unlabelled. This minimizes any effects that might alter the biochemical properties and structure of Impβ. The degree of labelling was 2.8 dyes per Impβ.

Fabrication of solid-state nanopores. The devices consisted of a nanometre-sized hole in a thin silicon nitride (SiN) membrane[3,21]. Briefly, a thin layer of SiN was deposited on a silicon (100) wafer, followed by electron-beam lithography, reactive ion etching and a KOH wet etch to create a 20 nm thin free-standing membrane of low-stress SiN. The free-standing membrane was then placed in a transmission electron microscope (TEM) operated at 300 kV. Formation of a nanopore resulted from the exposure of the membrane to a tightly focused electron beam. The diameter of the pore could be tuned with subnanometre accuracy with direct visual feedback[21]. For this study, we used pores ranging in diameter from 10 to 85 nm. After drilling, the pores were stored in a solution containing 50% ethanol and 50% ddH_20. A more detailed description of the nanopore fabrication process is given elsewhere[41].

Chemical modification of solid-state nanopores. The surface treatment used to immobilize Nups at the pore is schematically depicted in Supplementary Fig. S1. Both sides of the sample were subjected to oxygen plasma for ~30 s. This process removed any organic contaminants and resulted in oxidation of the surface, yielding SiO_2. The membranes were then (step 1) immersed into a 5% solution of (aminopropyl)triethoxysilane (APTES; obtained from Pierce) in pure methanol for 3–6 h, followed by rinsing for 10–15 min in pure methanol, drying under N_2 and baking at 100 °C for 30 min. This left exposed amine groups[42]. Subsequently (step 2), the amine groups were activated with a water-soluble, non-cleavable heterobifunctional crosslinker sulphosuccinimidyl-4-(*N*-maleimidomethyl)cyclohexane-1-carboxylate (sulfo-SMCC; 2 mg powder tablets were obtained from Pierce) to introduce maleimide groups. The crosslinkers had an amine-reactive NHS-ester (NHS esters react with primary amines at pH 7–9 to form stable amide bonds), in addition to a thiol-reactive maleimide (maleimides react with sulphhydryl groups at pH 6.5–7.5 to form stable thioether bonds). 'No-weigh' powder tablets (2 mg) of sulfo-SMCC were dissolved in 1.5 ml phosphate-buffered saline (PBS), pH 7.2. Membranes were then immersed overnight in the resulting solution. Subsequently, they were rinsed with Milli-Q filtered water (Millipore), acetone, ethanol, 2-isopropanol and Milli-Q again. In parallel, Nup98 and Nup153 were dialysed from buffer containing 8 M urea into PBS, and 1 mM of TCEP was added into their solutions for 30 min to reactivate the SH-groups. Finally, each membrane was incubated for 3 h in solutions containing 3 μg Nup98 or Nup153 (step 3), which attached to the pore via the maleimide moieties. Ellipsometry on coated SiN membranes confirmed the presence of the three layers.

Data acquisition and analysis. Ionic currents were detected by Ag/AgCl electrodes connected to an amplifier operating in resistive feedback mode (Axopatch 200B, Axon Instruments). All ion current measurements were performed at 150 mM KCl and 10 mM Tris-HCl, pH 8.0. Current traces were measured at a bandwidth of 100 kHz and digitized at 500 kHz. When necessary, low-pass filtering was applied: bare pore data were low-pass-filtered at 5 kHz, and Nup-coated pore data at 2 kHz. The upper trace in Fig. 3b was low-pass-filtered at 0.5 kHz for display purposes. The concentrations used in the nanopore experiment were 4.2 μM for BSA and 2.9 μM for Impβ (13 μM for the experiment with the array). The selectivity measurements were all performed with pores with dimensions of 44 ± 2 nm. The event-fitting algorithm used to analyse and label the translocation events was the same as one described elsewhere[32]. Error bars mentioned in the text denote the standard deviation of the distribution. Only events exceeding six times the standard deviation of the open-pore root-mean-square noise were considered. To avoid the effects of possible baseline fluctuations, we also limited ourselves to events for which the current before and after the event did not change more than 10% of the event amplitude.

Importin-β TIRF imaging. Glass microscope cover slips (22 × 22 mm, no. 1) were incubated with Poly-L-lysine solution (0.1% (w/v), Sigma-Aldrich) for 5 min and washed with PBS. A solution with Alexa-Fluor488-labelled Importin-β (Impβ-Alexa488), extracted from a diluted solution or from the trans-chamber in the translocation experiment, was then added at indicated concentrations and allowed to non-specifically adhere to the coated cover slips for 30 min. Following this, the fluorescence from individual molecules was detected by a TIRF microscope. The fluorescence signals from these surface-anchored Impβ were excited with a 491 nm diode-pumped solid-state laser (Cobolt) in a total internal reflection geometry, and fluorescence emission from Alexa-488 was detected with a ×60, 1.45 NA, oil immersion objective (Olympus), filtered with a 525/50 filter (Chroma Technology) and imaged onto a CCD camera (Andor iXon 897). Custom-written software was then used to identify single Impβ proteins on the cover slip and to monitor the Alexa-488 fluorescence at these positions.

Received 15 February 2011; accepted 17 May 2011; published online 19 June 2011

References

1. Alberts, B. *et al. Molecular Biology of the Cell* 5th edn (Garland Science, 2008).
2. Jovanovic-Talisman, T. *et al.* Artificial nanopores that mimic the transport selectivity of the nuclear pore complex. *Nature* **457,** 1023–1027 (2009).
3. Dekker, C. Solid-state nanopores. *Nature Nanotech.* **2,** 209–215 (2007).
4. Wente, S. R. Gatekeepers of the nucleus. *Science* **288,** 1374–1377 (2000).
5. Alber, F. *et al.* The molecular architecture of the nuclear pore complex. *Nature* **450,** 695–701 (2007).
6. Denning, D. P., Patel, S. S., Uversky, V., Fink, A. L. & Rexach, M. Disorder in the nuclear pore complex: the FG repeat regions of nucleoporins are natively unfolded. *Proc. Natl Acad. Sci. USA* **100,** 2450–2455 (2003).
7. Strawn, L. A., Shen, T., Shulga, N., Goldfarb, D. S. & Wente, S. R. Minimal nuclear pore complexes define FG repeat domains essential for transport. *Nature Cell Biol.* **6,** 197–206 (2004).
8. Rout, M. P. *et al.* The yeast nuclear pore complex: composition, architecture and transport mechanism. *J. Cell Biol.* **148,** 635–651 (2000).
9. Rout, M. P., Aitchison, J. D., Magnasco, M. O. & Chait, B. T. Virtual gating and nuclear transport: the hole picture. *Trends Cell Biol.* **13,** 622–628 (2003).
10. Lim, R. Y. H. *et al.* Nanomechanical basis of selective gating by the nuclear pore complex. *Science* **318,** 640–643 (2007).
11. Frey, S., Richter, R. P. & Görlich, D. FG-rich repeats of nuclear pore proteins form a three-dimensional meshwork with hydrogel-like properties. *Science* **314,** 815–817 (2006).
12. Frey, S. & Görlich, D. A saturated FG-repeat hydrogel can reproduce the permeability properties of nuclear pore complexes. *Cell* **130,** 512–523 (2007).
13. Peters, R. Translocation through the nuclear pore complex: selectivity and speed by reduction-of-dimensionality. *Traffic* **6,** 421–427 (2005).
14. Yamada, J. *et al.* A bimodal distribution of two distinct categories of intrinsically disordered structures with separate functions in FG nucleoporins. *Mol.Cell. Proteomics* **9,** 2205–2224 (2010).
15. Lowe, A. R. *et al.* Selectivity mechanism of the nuclear pore complex characterized by single cargo tracking. *Nature* **467,** 600–603 (2010).

© 2011 Macmillan Publishers Limited. All rights reserved.

16. Caspi, Y., Zbaida, D., Cohen, H. & Elbaum, M. Synthetic mimic of selective transport through the nuclear pore complex. *Nano Lett.* **8,** 3728–3724 (2008).
17. Lakshmi, B. & Martin, C. R. Enantioseparation using apoenzymes immobilized in a porous polymeric membrane. *Nature* **388,** 758–760 (1997).
18. Lee, S. B. *et al.* Antibody-based bio-nanotube membranes for enantiomeric drug separations. *Science* **296,** 2198–2200 (2002).
19. Kohli, P. *et al.* DNA-functionalized nanotube membranes with single-base mismatch selectivity. *Science* **305,** 984–986 (2004).
20. Lim, R. Y. H., Aebi, U. & Stoffler, D. From the trap to the basket: getting to the bottom of the nuclear pore complex. *Chromosoma* **115,** 15–26 (2006).
21. Storm, A. J., Chen, J. H., Ling, X. S., Zandbergen, H. W. & Dekker, C. Fabrication of solid-state nanopores with single-nanometre precision. *Nature Mater.* **2,** 537–540 (2003).
22. Jin, L., Horgan, A. & Levicky, R. Preparation of end-tethered DNA monolayers on siliceous surfaces using heterobifunctional cross-linkers. *Langmuir* **19,** 6968–6975 (2003).
23. Bustamante, J. O., Liepnis, A., Prendergast, R. A., Hanover, J. A. & Oberleithner, H. Patch clamp and atomic force microscopy demonstrate TATA-binding protein(TBP) interactions with the nuclear pore complex. *J. Membr. Biol.* **146,** 263–272 (1995).
24. Danker, T. *et al.* Nuclear hourglass technique: an approach that detects electrically open nuclear pores in Xenopus laevis oocytes. *Proc. Natl Acad. Sci. USA* **96,** 13530–13535 (1999).
25. Smeets, R. M. M., Keyser, U. F., Dekker, N. H. & Dekker, C. Noise in solid-state nanopores. *Proc. Natl Acad. Sci. USA* **105,** 417–421 (2008).
26. Siwy, Z. & Fulinski, A. Fabrication of a synthetic nanopore ion pump. *Phys. Rev. Lett.* **89,** 198103 (2002).
27. Hall, J. E. Access resistance of a small circular pore. *J. Gen. Physiol.* **66,** 531–532 (1975).
28. Ma, J. & Yang, W. Three-dimensional distribution of transient interactions in the nuclear pore complex obtained from single-molecule snapshots. *Proc. Natl Acad. Sci. USA* **107,** 7305–7310 (2010).
29. Moussavi-Baygi, R., Jamali, Y., Karimi, R. & Mofrad, M. R. K. Biophysical coarse-grained modeling provides insights into transport through the nuclear pore complex. *Biophys. J.* **100,** 1410–1419 (2011).
30. Fologea, D., Ledden, B., McNabb, D. S. & Li, J. Electrical characterization of protein molecules by a solid-state nanopore. *Appl. Phys. Lett.* **91,** 053901 (2007).
31. Yang, W. & Musser, S. M. Nuclear import time and transport efficiency depend on importin β concentration. *J. Cell Biol.* **174,** 951–961 (2006).
32. Storm, A. J., Chen, J. H., Zandbergen, H. W. & Dekker, C. Translocation of double-strand DNA through a silicon oxide nanopore. *Phys. Rev. E.* **71,** 051903 (2005).
33. Dange, T., Grünwald, D., Grünwald, A., Peters, R. & Kubitscheck, U. Autonomy and robustness of translocation through the nuclear pore complex: a single-molecule study. *J. Cell Biol.* **183,** 77–86 (2008).
34. Yang, W. D., Gelles, J. & Musser, S. M. Imaging of single-molecule translocation through nuclear pore complexes. *Proc. Natl Acad. Sci. USA* **101,** 12887–12892 (2004).
35. Kubitscheck, U. *et al.* Nuclear transport of single molecules: dwell times at the nuclear pore complex. *J. Cell Biol.* **168,** 233–243 (2005).
36. Kowalczyk, S. W., Hall, A. R. & Dekker, C. Detection of local protein structures along DNA using solid-state nanopores. *Nano Lett.* **10,** 324–328 (2010).
37. Zilman, A., Di Talia, S., Chait, B., Rout, M. & Magnasco, M. Efficiency, selectivity and robustness of the transport through the nuclear pore complex. *PLoS Comput. Biol.* **3,** e125 (2007).
38. Zilman, A. *et al.* Enhancement of transport selectivity through nano-channels by non-specific competition. *PLoS Comput. Biol.* **6,** e1000804 (2010).
39. Keyser, U. F. *et al.* Direct force measurements on DNA in a solid-state nanopore. *Nature Phys.* **2,** 473–477 (2006).
40. Strelkov, S. V., Kreplak, L., Herrmann, H. & Aebi, U. Intermediate filament protein structure determination. *Meth. Cell Biol.* **78,** 25–43 (2004).
41. Krapf, D. *et al.* Fabrication and characterization of nanopore-based electrodes with radii down to 2 nm. *Nano Lett.* **6,** 105–109 (2006).
42. Wanunu, M. & Meller, A. Chemically modified solid-state nanopores. *Nano Lett.* **7,** 1580–1585 (2007).

Acknowledgements

The authors thank K.A. Williams for suggestions on the chemistry, A.R. Hall, M. van den Hout and X. Janssen for membrane fabrication and discussions, D. Grünwald and G.V. Soni for help with TIRF measurements, Y. Rabin and A.Y. Grosberg for help with theoretical work, and T. Dange, N.H. Dekker, D. Grünwald, P.L. Hagedoorn, G.F. Schneider and G.M. Skinner for discussions. This research was funded by the 'Nederlandse Organisatie voor Wetenschappelijk Onderzoek (NWO)', programme NanoSci E+ of the European Commission, and the READNA (REvolutionary Approaches and Devices for Nucleic Acid analysis) project of the European Commission. L.K. and R.Y.H.L. are supported by the National Center of Competence in Research 'Nanoscale Science' (NCCR-Nano), the Swiss National Science Foundation, the Biozentrum and the Swiss Nanoscience Institute.

Author contributions

S.W.K., R.Y.H.L. and C.D. devised the experiments. L.K. cloned, purified and labelled proteins and carried out SPR analysis. S.W.K., T.R.B., T.M. and P.V.N. carried out the experiments and analysed data. S.W.K., R.Y.H.L. and C.D. wrote the manuscript.

Additional information

The authors declare no competing financial interests. Supplementary information accompanies this paper at www.nature.com/naturenanotechnology. Reprints and permission information is available online at http://www.nature.com/reprints/. Correspondence and requests for materials should be addressed to R.Y.H.L. and C.D.

© 2011 Macmillan Publishers Limited. All rights reserved.